Computational Condensed Matter 39 (2024) e00911

Contents lists available at ScienceDirect

Computational Condensed Matter

journal homepage: www.elsevier.com/locate/cocom

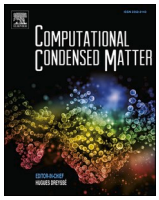

Structural, phonon, optical, electronic, and thermodynamic properties of NpX (X = S, Se, Te) chalcogenides: A DFT study

Abu Bakar [a], Sadam Hussain [a], Ghulam M. Mustafa [b,*], Rana Ali Ahmad [c], Abdul Quader [d], Muhammad Imran [b], Ibrahim A. Shaaban [e]

[a] Centre of Excellence in Solid State Physics, University of the Punjab, Lahore, 54590, Pakistan
[b] Department of Physics, Division of Science and Technology, University of Education, Lahore, Punjab, 54770, Pakistan
[c] University of Science and Technology of China, Hefei, Anhui, 230026, People's Republic of China
[d] Institute of Physics, The Islamia University of Bahawalpur, Bahawalpur, Pakistan
[e] Department of Chemistry Faculty of Science King Khalid University, Abha, 61321, Saudi Arabia

ARTICLE INFO

Keywords:
Binary chalcogenides
Optical constants
Reststrahlen band
IR devices
Thermodynamic

ABSTRACT

Binary chalcogenides with small Reststrahlen bands in the far infrared and microwave region make them intriguing for IR sensors and radar communication purposes. In this study, we have theoretically investigated the structural, phonon, electronic, optical, IR optical and thermodynamic properties of NpX, where X = S, Se, and Te chalcogenides. The face-centered cubic structure is relaxed to determine the optimized lattice parameters which increased with an increase in the size of involving chalcogen atom. Band structure reveals their metallic nature. The significant contribution of *d* and *f*-states of Np and *p*-states of chalcogens in band formation is evident from the density of state plots. The detailed analysis of optical parameters including real and imaginary parts of dielectric constant and refractive index, optical conductivity, and optical loss exhibit high absorption in the IR region.

1. Introduction

Reststrahlen bands are a phenomenon that occurs in certain materials, particularly those that have strong ionic bonding, and originates from the interaction of electromagnetic radiation with the vibrational modes of the crystal lattice. The understanding of Reststrahlen bands can play a pivotal role in the development of optoelectronic devices, particularly in the areas of infrared optics and thermal imaging [1,2]. Infrared radiations have wavelengths in the range of 0.78–1000 μm and can be used for a variety of purposes, including thermal imaging, remote sensing, and communication [3,4]. Materials that exhibit Reststrahlen bands are particularly well-suited for use in infrared optics because they can absorb and reflect infrared radiation with high efficiency. The Reststrahlen bands are typically located in the far-infrared region of the spectrum, which makes them ideal for use in thermal imaging devices [5]. For instance, SiC is a semiconductor material that has strong ionic bonding and exhibits Reststrahlen bands in the far-infrared region of the spectrum and therefore, has potential for infrared devices [6]. Thermal imaging is the process of using infrared radiation to create images of objects based on their temperature and can be used in a variety of applications, including medical imaging, security, and surveillance [7]. In addition, such materials can be used to create optical filters for enhancing the sensitivity and resolution of thermal imaging devices [8]. Likewise, the corresponding frequency of Reststrahlen bands lies in the terahertz range therefore, these materials are also good for security screening, medical imaging, and communication. $LiNbO_3$ is a ferroelectric material that has strong ionic bonding and exhibits Reststrahlen bands in the terahertz region and therefore, is an excellent material for use in IR radiation sources and detectors [9,10].

Chalcogenides have unique physical and chemical properties that make them useful in various applications, including electronics, optoelectronics, and energy storage [11]. Small bandgaps in chalcogenides make them suitable for electronic devices such as photovoltaic cells, light-emitting diodes (LEDs), and field-effect transistors (FETs) [12]. In addition, these materials can be used in the production of optical fibers, which are used in telecommunications and data transmission [13]. They can also be used in rechargeable batteries, including lithium-sulfur batteries, which have high energy densities and long cycle lives [14]. Particularly, Se and Te-based compositions have a high potential to convert heat into electricity and therefore are suitable thermoelectric

* Corresponding author.
E-mail address: gmmustafa25@gmail.com (G.M. Mustafa).

https://doi.org/10.1016/j.cocom.2024.e00911
Received 9 December 2023; Received in revised form 23 April 2024; Accepted 25 April 2024
Available online 28 April 2024

materials [15].

Recently, sulfide-based chalcogenides have been studied widely, and different researchers suggest considering them as potential materials for solar cells and optoelectronics. The optical constants and electronic band structures of such chalcogenides were studied both theoretically and experimentally by Vu et al. In particularly, a direct band gap for quaternary copper mercury tin sulfide was reported [16]. However, in the case of quaternary silver lead germanium sulfide an indirect band gap was reported in which the 3p states of S contribute to the upper portion of valence band [17]. From the start of the 21st century, different compositions of selenides and sulfides-based chalcogenides were investigated and considered attractive materials to be utilized as absorber layers of solar cells as well as for optoelectronic applications [18]. Quaternary silver mercury tin selenide was studied both theoretically and experimentally by Vu et al. who reported a 1.24 eV band gap which is considered a potential candidate for solar cell application [19]. Gabrelian et al. investigated the optical and electronic structure of quaternary telluride and reported a 0.282 eV band gap [20]. Based on the above literature review, it can be noted that sulfide, selenide, and telluride chalcogenides recently gained much attention in the optoelectronic industry due to their unique properties. These materials have shown promise for use in a variety of optoelectronic devices, including solar cells, photodetectors, and light-emitting diodes (LEDs). They also have a lower thermal conductivity and thus can retain more of the absorbed energy as electrical energy [21]. They can be fabricated at lower temperatures than silicon, which makes the manufacturing process more energy-efficient. Research has shown that these chalcogenides can be used as the absorber layer in solar cells, replacing the traditional silicon absorber layer [22].

Reststrahlen band study grabbed increasing interest in recent times due to the interesting physics involved and the placement of possible applications in technologically advanced research areas. For instance, Kowalski et al. investigated the Hf-based transition metal dichalcogenides which supported the surface phonon polaritons in the infrared region. The transmission and reflectance IR spectra of HfS_2 and $HfSe_2$ were calculated from which dielectric functions were derived. The Reststrahlen bands exceptionally expanded originated from the sevenfold increase Born effective charge of Hf-based compounds [23]. Heβler et al. studied the switchable, ultra-thin infrared absorbers formed by the thin films of chalcogenides phase change materials. These materials exhibited a high contrast between highly lossy crystalline materials and lossless amorphous materials. They exceptionally tuned the absorption of maximum wavelength up to 2.5 μm by annealing and optical switching and demonstrated that lossy phase change materials are potential candidates for reconfigurable and ultra-thin nanophotonic devices [24]. Valakh et al. theoretically and experimentally investigated the Ge/Sn-substituted Cu_2ZnSnS_4 single crystal and observed two mode transformations in the vibrational modes and a small dispersion in the Brillouin zone which is typical for a molecular crystal. These modes of vibrations are attributed to the breathing of S inside GeS_4 and SnS_4 tetrahedra [25]. In the present work, we have selected three chalcogenide compositions NpX (X = S, Se, Te) to explore their structural, electronic, optical, phonon, and thermodynamic properties. The phonon dispersion curves will further be used to find the reststrahlen bands and hence the possible applications in infrared (IR) and far infrared (FIR) regions of the spectrum which reveal the potential of these compositions for IR devices and communication devices.

2. Computational details

Evaluation of density functional theory (DFT) generates new tools to calculate the phonon properties with higher accuracy [26]. DFT embodied in WIEN2k code with Full Potential Linearized Plane Wave (FP-LAPW) method [27] is used to find electronic, optical properties of NpX. Phonon, and thermodynamic, properties are also studied with Quantum ESPRESSO [28], and Gibbs2, codes respectively. The calculated phonon dispersion curves are further used to compute the reststrahlen band of the under-study materials. Within the framework of Perdew–Burke–Ernzerhof Generalized Gradient Approximation (PBE-GGA), the interaction between valence and core electrons was elaborated [29]. The electronic band structures are also tested by using some corrections with PBE like PBE with spin-orbit coupling, PBE with Hubbard potential and TB-mBJ. The plane wave number was controlled by the $R_{MT} \times K_{\max}$ parameter which is set as 7.0. The core and valence states were separated by value −6.0Ry of cut-off energy. The 120 k-points were generated in irreducible BZ which was distributed in a $20 \times 20 \times 20$ grid of Monkhorst Pack [30] in irreducible BZ. The charge and energy convergence criteria were set to 0.0001e and 0.00001Ry respectively. The Fourier expansion coefficient of charge density and maximum angular momentum were set to $G_{\max} = 12$ & $l_{\max} = 10$, respectively. For phonon properties, the charge densities were extended to 480 and 320 Ry with the cut of energies of 120 and 80 Ry respectively. For modeling of Brillouin zone, a 4x4x4Monkhorst–Pack meshing of k points was set with the convergence threshold of 10^{-6} for all compositions [30].

3. Results and discussion

3.1. Energy volume optimization

The energy-volume optimization graph showcases the relationship between the volume of the crystal lattice and the corresponding total energy of the compounds. This graph provides insights into the stability and structural properties of these materials. These graphs for NpS, NpSe, and NpTe compositions are displayed in Fig. 1 where it has been witnessed that the energy of the system changes with a change in the volume of the system. The energy-volume curve typically exhibits a parabolic shape, indicating that there is an optimal volume at which the system attains its lowest energy state. This volume corresponds to the lowest energy leading to determining the most stable configuration and optimized lattice constants. This configuration is the most energetically favorable because as the volume deviates from this configuration, energy increases indicating the reduction of structural stability. It is important to note that the specific shape of the energy-volume curve depends on various factors, including the interatomic interactions, bonding characteristics, and crystal structure of the materials. The unique electronic and structural properties of each compound (NpS, NpSe, and NpTe) contribute to the distinctive shapes of their respective energy-volume optimization graphs. The value of the lattice parameter is noted as 5.3770 Å for NpS which increased to 5.6168 and 6.0525 Å when S is substituted with Se and Te. This increase in lattice parameter is associated with the increasing ionic radii of Se (1.98 Å) and Te (2.21 Å) as compared with S (1.84 Å). The corresponding value of bulk modulus noticed in structure optimization was 125.0451, 100.3938, and 80.7257 GPa for NpS, NpSe, and NpTe, respectively. This variation in structural parameters would significantly affect the electronic, optical, and transport properties of these materials.

3.2. Energy band structure

The energy band structure is a key factor used to define different physical and optical properties of materials. The energy band structure of NpS using PBE-GGA, TB-mBJ, PBE + SOC, and PBE + U is presented in Fig. 2 (a, b, c, d). It has been noticed that the distribution of energy states in bands along different symmetry directions in the Brillouin zone is not uniform. This is because, within a crystal, the arrangement of atoms creates a periodic potential that affects the behavior of electrons. This potential gives rise to energy bands, which represent the allowed energy states for electrons in the crystal lattice. Since the distribution of energy states within a band is determined by the crystal's symmetry and periodicity. From the figure, it is evident that NpS exhibited no bandgap and thus exhibited a metallic character. This difference in band structure

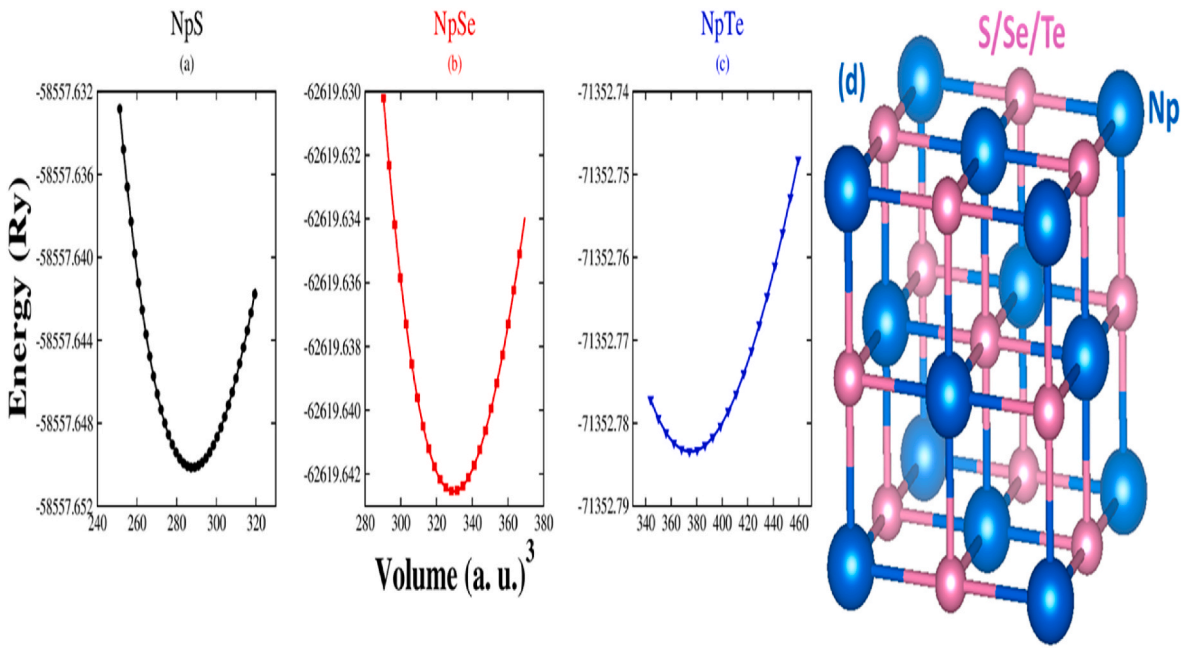

Fig. 1. (a–c) Energy-volume optimization graphs and (bd) unit cell of NpX (X = S, Se, Te).

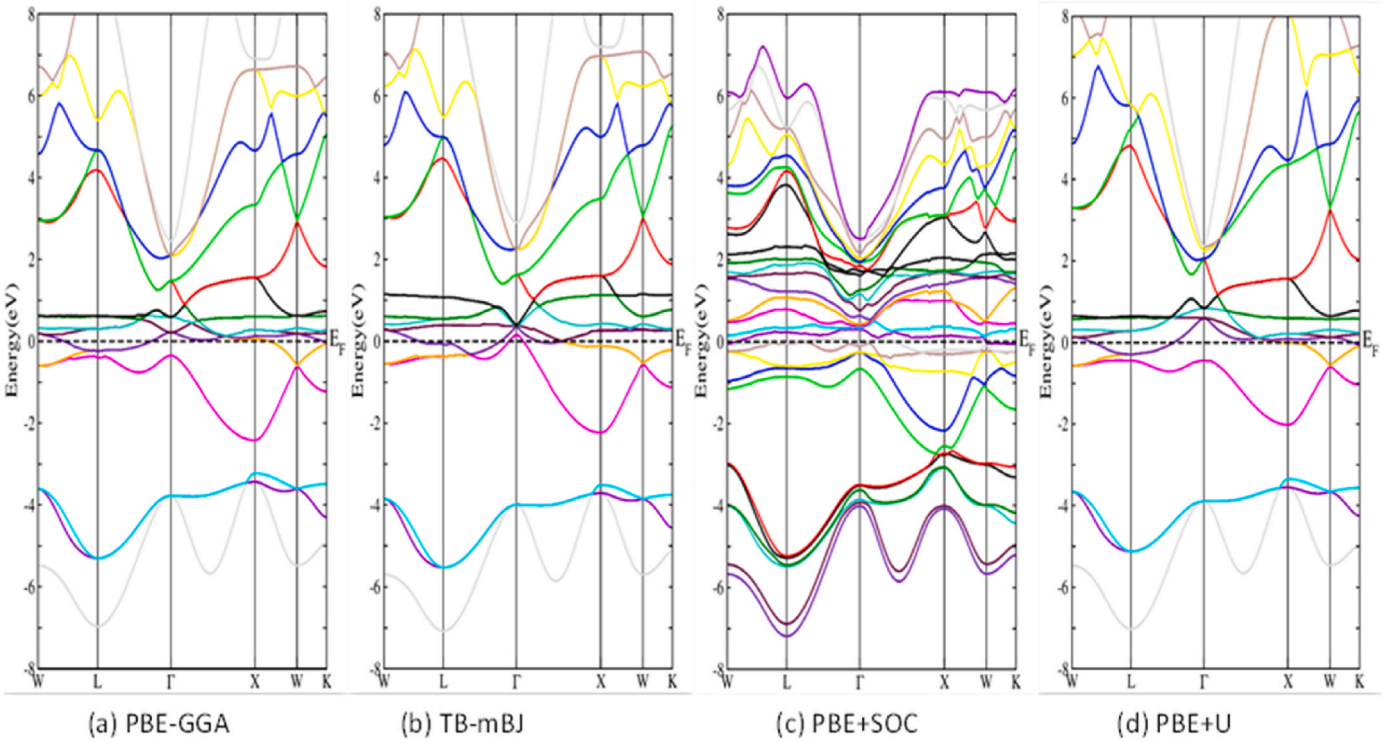

Fig. 2. Band structure of NpS explored by different methods.

arises due to the presence of spin-orbit coupling and the resulting spin-dependent electronic structure [31]. Almost similar behavior was evidenced for NpSe and NpTe compositions as shown in Fig. 3 (a, b, c, d) and Fig. 4 (a, b, c, d). This conducting behavior is attributed to the relatively high density of states at the Fermi level. In other words, there are plenty of available energy states for electrons with the majority spin orientation, which allows them to move through the material more easily, resulting in high electrical conductivity. This overlapping of states across the Fermi level could involve the interplay of various factors, such as the crystal field splitting, hybridization between different atomic orbitals, and spin-dependent interactions [32].

3.3. *Density of state plots*

In the spin-up channel (majority spin orientation), the total DOS plot for NpS as a conductor would show a significant number of available electronic states across the Fermi level. The plot typically exhibits broad peaks, reflecting the relatively high density of electronic states.

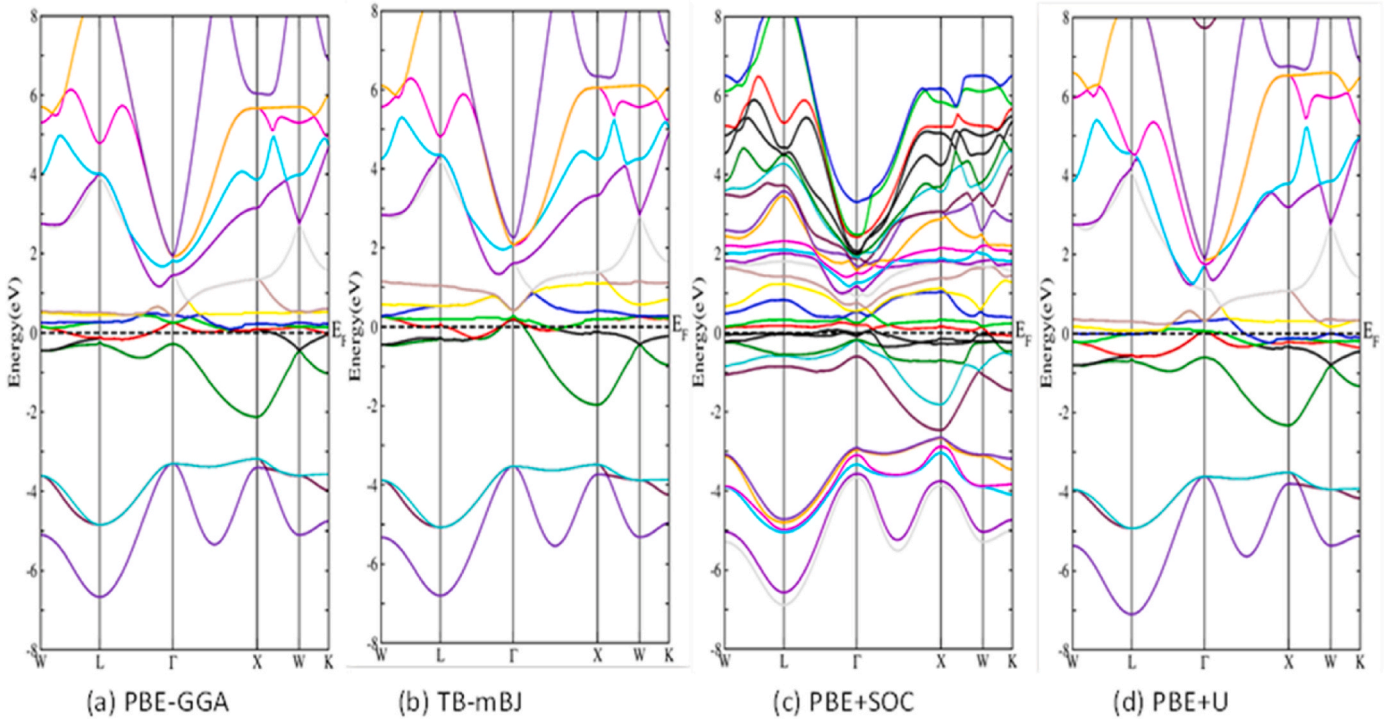

Fig. 3. Band structure of NpSe explored by different methods.

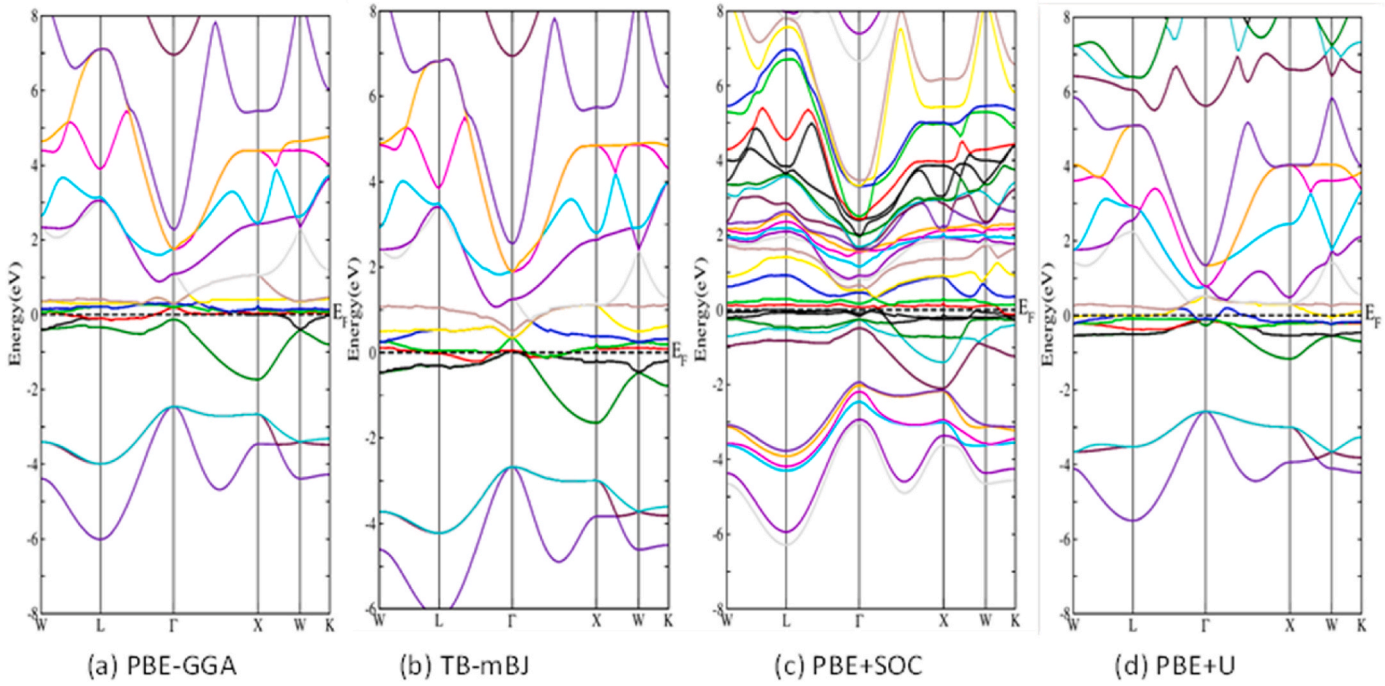

Fig. 4. Band structure of NpTe explored by different methods.

Therefore, there are numerous energy levels that electrons with the majority spin can occupy. As a result, these electrons can move freely through the material, contributing to its high electrical conductivity. The total density of states (TDOS) and partial density of states (PDOS) plots for the studied compositions are provided in Figs. 5 and 6. These results support the findings of band structure. In the (↑) channel, the presence of broad peaks at the Fermi level reflects a relatively high density of electronic states indicating the conducting nature of these compositions whereas in the (↓) orientation, the energy states touch the Fermi level from the valence band. Energy states in the conduction band in the (↓) channel spread from 1 to 4 eV. The partial density of states (PDOS) plot is a representation of the electronic density of states for specific atomic orbitals within a material and provides valuable insights into the electronic structure of the material, showing how the energy levels are distributed among different orbitals of various atomic species. In the case of NpS, the plot shows the distribution of electronic states for

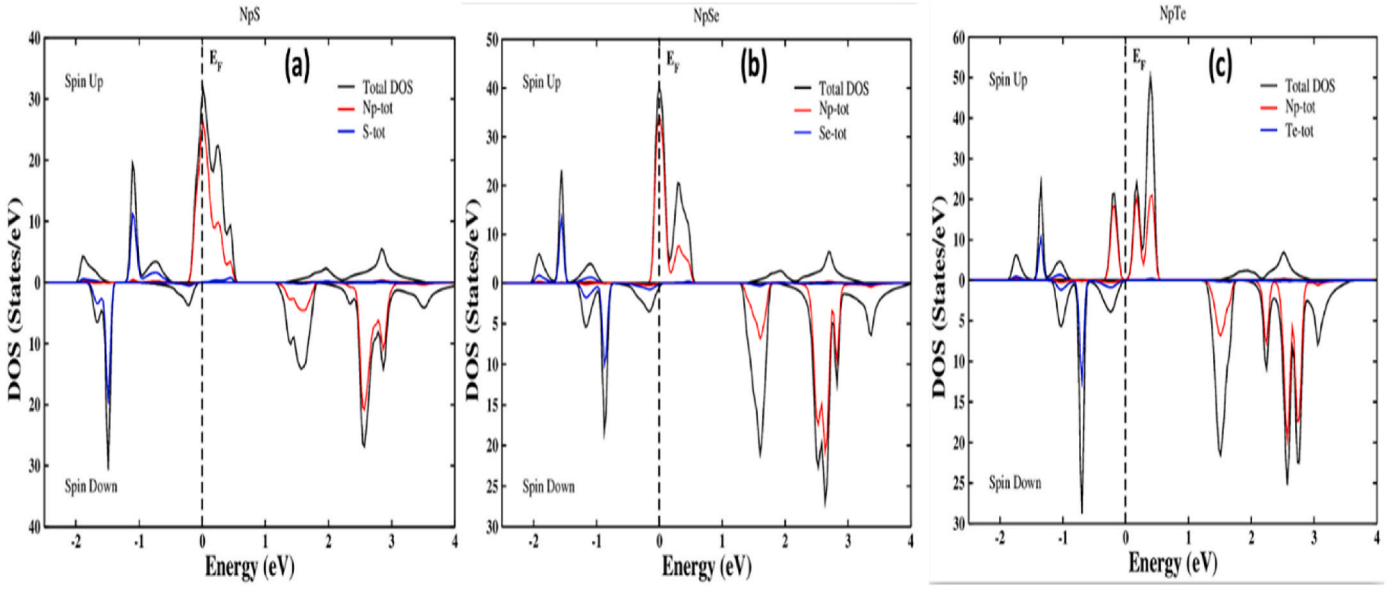

Fig. 5. Total density of states of NpX (X = S, Se, Te) in spin-up and spin-down channels.

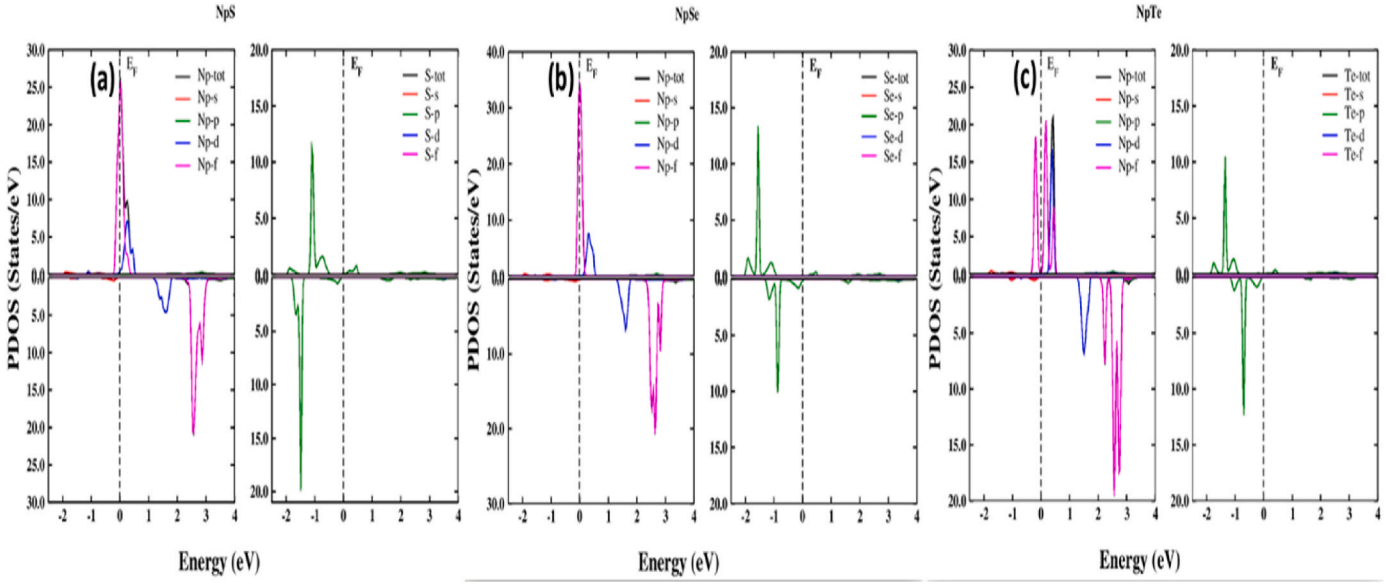

Fig. 6. Partial density of states of NpX (X = S, Se, Te) in spin-up and spin-down channels.

neptunium (Np) and sulfur (S) atoms separately. Np is a f-block actinide element, while S is a chalcogen element. Since NpS is a compound of these two elements, the PDOS plot reflects the contribution of both Np and S to the overall electronic structure of the material. In the case of NpSe, NpTe, the overall density of states increased indicating a greater number of electrons available in Se and Te as compared with S. However, in the (↓) channel, the TDOS decreased with the increase in size of the involved chalcogen. The different responses in both spin channels make these compositions viable for spintronic applications [33].

3.4. Phonon properties and reststrahlen band investigations

Fig. 7(a) shows the phonon dispersion curve for NpS chalcogenide witnessing the presence of six modes of vibration including three acoustic modes in which two are transverse acoustics (TA) and one is longitudinal acoustic (LA) in addition to three optical modes of vibration in which two are transverse optical (TO) and one is longitudinal optical (LO) mode. The vibrational frequency of the TO phonon is recorded as 363.259 cm^{-1} and LO phonon is 374.962 cm^{-1} at X position. The splitting of phonon spectra in the first Brillion zone is attributed to the ionic polarizabilities and the absence of imaginary phonon frequency assures that the NpS material is dynamically stable [34]. We also noted from the above figure that there is a gap of frequencies between optical and acoustic modes of vibration in which a wave-like solution does not exist. The existence of this band indicates that it is not possible to excite phonon vibrations of the frequency lying within this band and for this reason, it is also called the forbidden frequency band and the width of this frequency band gap depends upon the difference of the masses of the atoms NpX (X = S, Se, Te) such that greater the mass difference greater will be the forbidden gap. The PDOS plot for NpS is presented in Fig. 7(b) which shows that maximum states occur in the frequency range of 348–375 cm^{-1} whereas in the range of about 130–345 cm^{-1} there is no state because this region is a forbidden frequency range where no phonon mode is vibrated for NpS and this forbidden frequency gap was

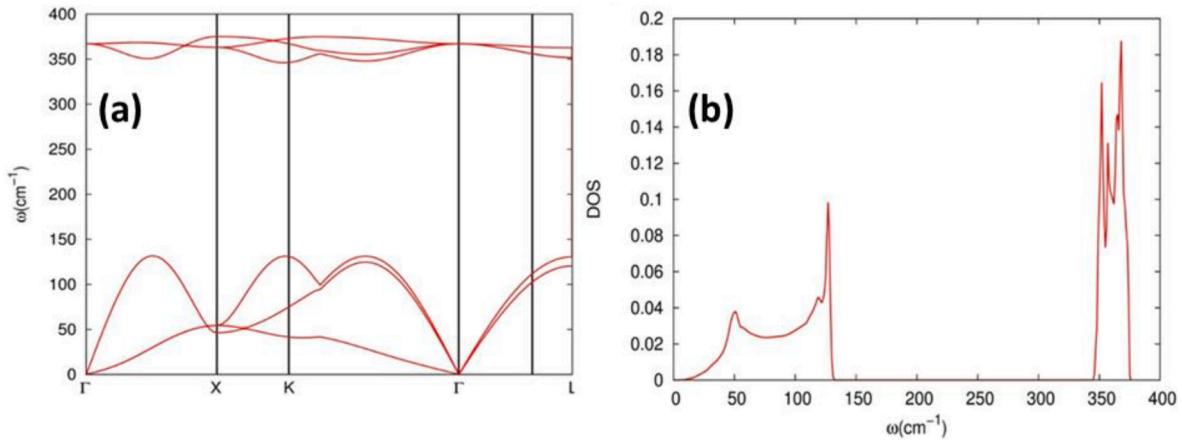

Fig. 7. **(a)** Phonon dispersion curves and **(b)** phonon density of states of NpS with PBE-GGA.

also investigated with the help of the dispersion cure of NpS.

The phonon dispersion curves and corresponding phonon density of states for NpSe and NpTe are presented in Fig. 8(a and b) and Fig. 9 (a, b) respectively. The same trend was observed for NpSe and NpTe with a difference that the band of optical phonons moves towards lower frequency and reduces the forbidden gap. This shifting of phonons of optical bands towards lower vibrating frequency is attributed to the increasing atomic weight of involving chalcogen atoms. Reststrahlen band is a region between ω_{TO} and ω_{LO} where the material acts as a 100 % reflector for incoming light. As we have seen earlier from the dispersion curves of the Neptunium-based chalcogenides LO phonon modes are overlapping at Γ the position of the first Brillion zone where no Reststrahlen band occurs. Therefore to find the Reststrahlen band for NpX (X = S, Se, Te) we take X position of the first Brillion zone to investigate the Reststrahlen band as below;

The data listed in Table 1 present that, the Reststrahlen bandwidth of NpX decreases down the group and is also dependent upon the difference of masses of the atoms. In the electromagnetic spectrum, the range of the Far-infrared region is (24.8–1.24) meV, and microwave is 1.24meV-1.24 μeV. The above-calculated values show that the Reststrahlen band of NpS material is lying in the FIR range which highlights the potential of these compositions for sensing applications in astrochemistry, biology, industrial, and geological processes. While the Reststrahlen band values of NpSe and NpTe are lying in the microwave range. Microwaves have a range of applications, including communications, radar, and microwave Ovens.

3.5. Optical properties

The real part of dielectric constant, (ε1) is a measure of how a material responds to an electric field in terms of its ability to store and release energy. It plays a significant role in understanding the optical and electronic properties of materials. The variation of ε1 in the energy range of 0–6 eV for NpS, NpSe, and NpTe is presented in Fig. 10(a) where a notable trend emerges with respect to the size of the chalcogen atoms (S, Se, and Te). As the size of the chalcogen atom increases from S to Se and Te, a significant shift in the major peak of the dielectric constant towards lower energy is observed. The shift in the major peak towards lower energy can be explained by considering the energy levels of the chalcogen p-orbitals. As the size of the chalcogen atom increases down the periodic table (from S to Se and Te), the energy difference between the valence p-orbital and the conduction band decreases. This leads to a decrease in the energy required to excite electrons from the valence band to the conduction band, resulting in a redshift of the absorption peak in the dielectric constant [35]. Additionally, the increase in chalcogen size can lead to changes in the electronic band structure, density of states, and interatomic bonding within the material. These changes can influence the way the material absorbs and interacts with light in the given energy range. Moreover, the increase in atomic size might introduce changes in the crystal lattice parameters, affecting the phonon modes and vibrational properties of the material, which can also contribute to the observed peak shifts.

The imaginary part of the dielectric constant (ε_2) plays a crucial role in describing the absorption and scattering of light by a material as a

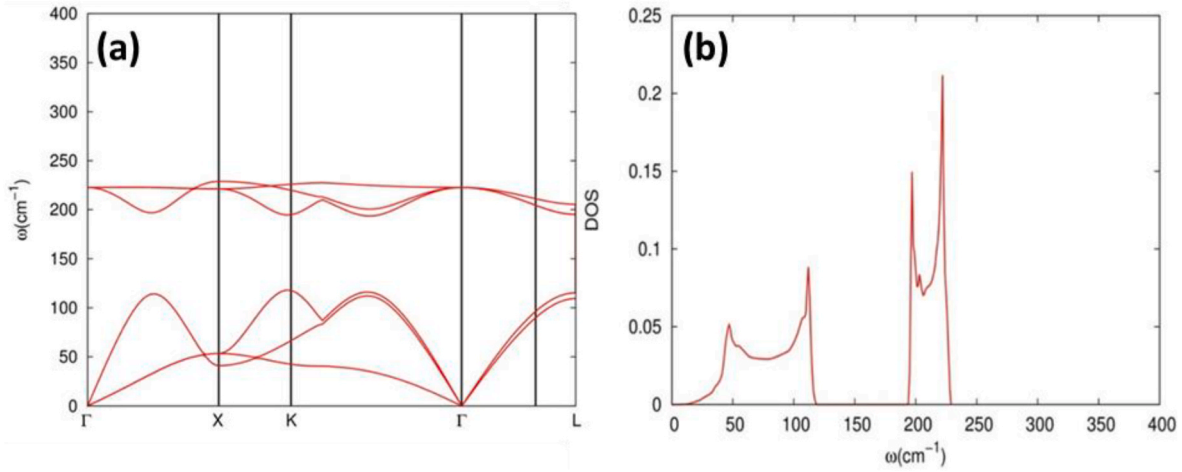

Fig. 8. **(a)** Phonon dispersion curves and **(b)** phonon density of states of NpSe with PBE-GGA.

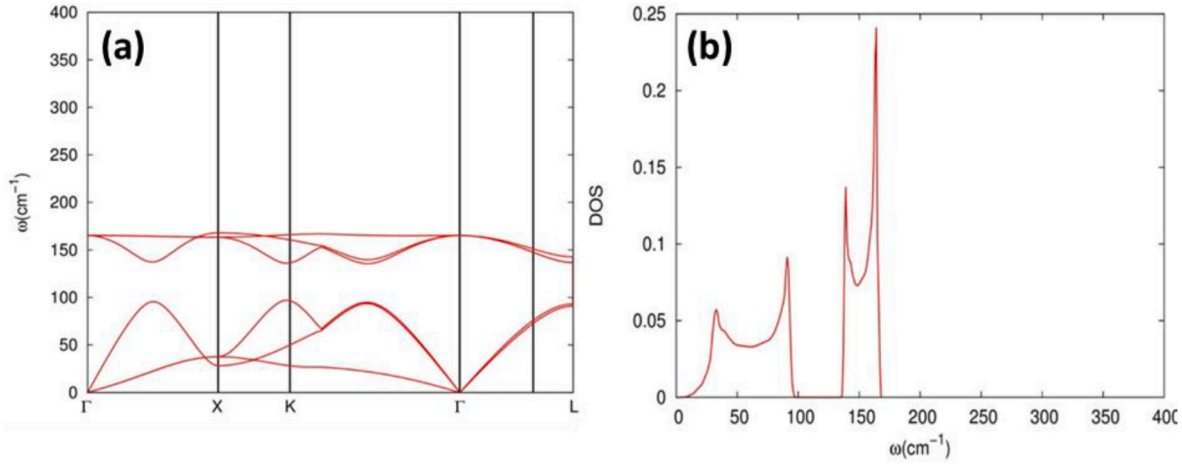

Fig. 9. **(a)** Phonon dispersion curves and **(b)** phonon density of states of NpTe with PBE-GGA.

Table 1
Calculated Reststrahlen band in NpX (X = S, Se, Te) at X position.

Materials	$\omega_{LO}(cm^{-1})$	$\omega_{TO}(cm^{-1})$	$\frac{\epsilon(0)}{\epsilon(\infty)} = \frac{\omega_{LO}^2}{\omega_{TO}^2}$	Reststrahlen Band			
				cm^{-1}	μm	THz	meV
NpS	374.962	363.259	1.065	11.703	854.481	0.35	1.45
NpSe	228.994	221.307	1.070	7.687	1300.897	0.23	0.953
NpTe	167.97	163.355	1.057	4.615	2166.847	0.138	0.572

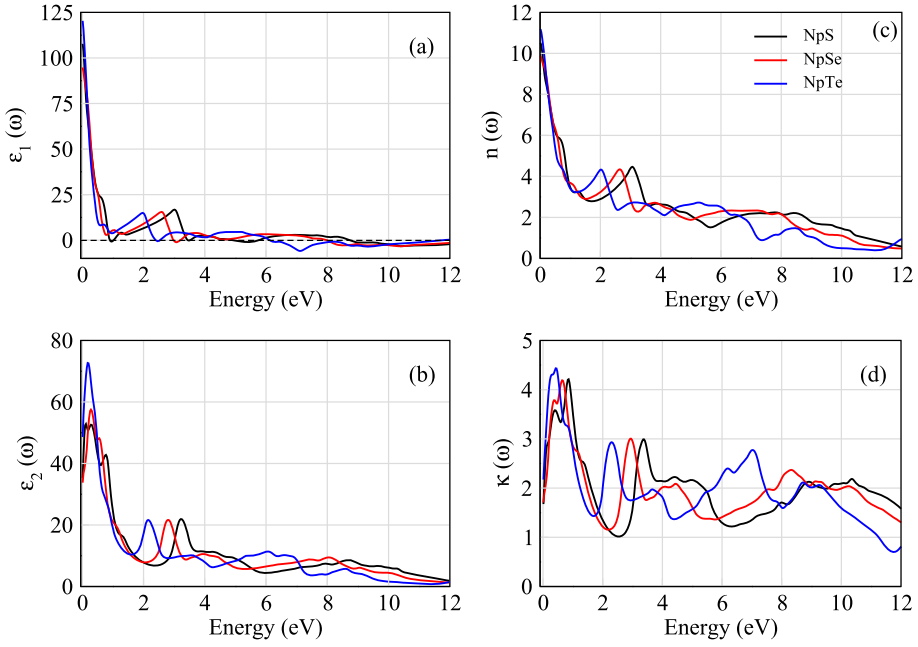

Fig. 10. (a) Real and (b) imaginary parts of dielectric constant, (c) refractive index, and (d) extinction coefficient of NpX (X = S, Se, Te).

function of energy for NpS, NpSe, and NpTe in the energy range of 0–6 eV that is plotted in Fig. 10(b) [36]. These compounds have intriguing properties due to their varying atomic sizes and electronic configurations. These differences in atomic properties lead to variations in the optical behavior of the compounds they form. In addition to these parameters, the refractive index (n) and extinction coefficient (k) are known to exhibit interesting optical behavior. As we move across the chalcogenide series from S to Se and Te, it has been observed that n and k followed the trend of ε_1 and ε_2 respectively. The refractive index measures the speed of light in a material relative to its speed in a vacuum. Therefore, it is related to the phase velocity of light within the material. Generally, for most materials, the value of n decreases with increasing photon energy, resulting in a gradually flatter curve of n versus E plot as shown in Fig. 10(c). This behavior is observed in all studied compositions. In addition, the extinction coefficient is linked to the absorption of light within a material and provides information about how strongly a material absorbs light at a given energy [37]. In the energy range of interest, the extinction coefficient exhibited distinct peaks or features, indicating absorption bands corresponding to certain electronic transitions (Fig. 10(d)). For chalcogenides, NpS, NpSe, and NpTe, these

transitions are likely due to electronic excitations involving the valence and conduction bands. One significant trend observed is that the positions of the major absorption peaks tend to shift towards lower energy as we move from smaller to larger chalcogen atoms which is attributed to changes in the electronic structure and the energy levels of the valence and conduction bands. Larger chalcogen atoms have more extended electron cloud distributions, leading to lower energy electronic transitions.

When studying the optical properties absorption spectra provide information about the energy levels at which the material absorbs light. The absorption spectrum is related to the imaginary part of the dielectric constant through the Kramers-Kronig relations [38]. The tuning of absorption coefficient with energy of incident photon is presented in Fig. 11(a). The redshift in absorption peaks with increasing chalcogen size can be attributed to changes in the electronic band structure and density of states. In larger chalcogen compounds like NpSe and NpTe, the increase in atomic size leads to a broader distribution of energy levels. This broader distribution results in a lower energy gap between the valence and conduction bands, allowing for the absorption of lower energy photons. Consequently, the major absorption peak shifts towards lower energies in the absorption spectrum. The optical conductivity variation of chalcogen compounds is presented in Fig. 11(b) exhibiting distinct behavior due to their unique electronic structures. NpS displayed a notable conductivity response in the visible to near-infrared range, attributed to its semiconducting nature and the involvement of sulfur-derived energy bands. In the case of NpSe, a smaller bandgap compared to NpS results in enhanced optical conductivity, particularly in the IR region. These variations underscore the significant influence of chalcogen composition on the optical properties of neptunium-based chalcogenides, enabling tailored applications in optoelectronic devices.

The variation of optical reflectivity R(ω) of NpS, NpSe, and NpTe is shown in Fig. 11(c) exhibiting multiple peaks at different energy values. The involved chalcogen atoms are semiconductors with narrow band gaps. This implies that they have limited conductivity at room temperature and are capable of absorbing and reflecting light within specific energy ranges. The value of R(ω) is closely linked to their energy band structure, where the energy difference between the valence and conduction bands determines their ability to absorb and reflect photons of varying energy levels. Optical loss factor L(ω) measures the reduction in the intensity of light as it propagates through a medium due to the absorption or scattering of light. The value of L(ω) is plotted against the energy of the incident photon in Fig. 11(d). Optical loss can occur due to various factors, including absorption of light by the material itself, scattering of light by particles or imperfections in the material, and other phenomena that cause the light energy to be converted into heat or other forms of energy. For the studied compositions, the local environment of neptunium atoms within the crystal lattice also plays a role in determining the optical loss characteristics. Defects, impurities, and crystal imperfections can introduce additional energy levels within the band gap, leading to absorption and scattering of photons. Understanding and controlling these factors are crucial for tailoring the optical properties of these materials for specific applications in areas such as optoelectronics, photovoltaics, and sensors.

3.6. Thermodynamic properties

As the material's thermal response may be calculated to explore its thermal properties, that's why thermodynamic calculations of neptunium-based chalcogenide compounds are considered unquestionably essential as this information will be helpful for future studies. So, thermodynamic properties of neptunium-based chalcogenides NpX with (X = S, Se, and Te) were performed using Quantum Harmonic Approximation (QHA) along Gibbs2 code. Fig. 12 shows the effect of temperature on volume at various pressures of 0, 5, and 10 GPa. The volume-dependent thermal effects are explained by the harmonic approximation, which has been proposed to accurately represent all the values of lattice parameters. The inverse effect of volume pressure can be noted for all the compounds. However, it can be seen that the volume of NpS and NpTe increase with the increase of temperature while the NpSe exhibits an inverse effect. The volume of NpSe chalcogenides decreases with the increase in temperature.

We attempt to explore the thermal properties of chalcogenides via the Quasi-Harmonic Debye (QHD) model as according to quantum statistical mechanics this model ensemble of harmonic oscillators. In the QHD model, Debye temperature is considered one of the key quantities that is correlated with other properties like thermal expansion, elastic constant, specific heat, and melting temperature. Fig. 13 shows the Debye temperature of NpX chalcogenides at various pressures of 0, 5, and 10 GPa by changing temperature.

An increase in Debye temperature was noted with the increase of

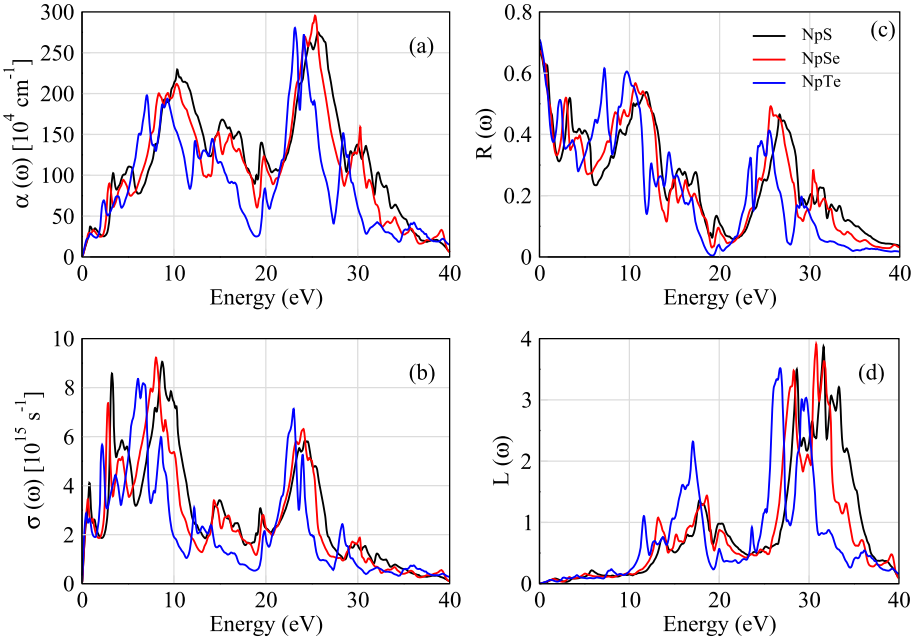

Fig. 11. (a) Absorption, (b) optical conductivity, (c) reflectivity, and (d) optical loss of NpX (X = S, Se, Te).

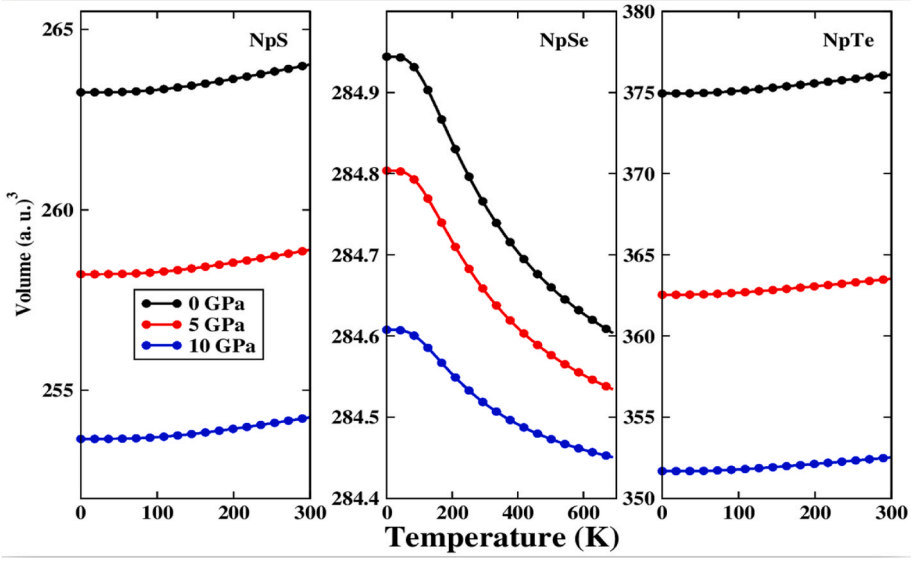

Fig. 12. The change in volume with temperature and pressure of NpX (X = S, Se, Te).

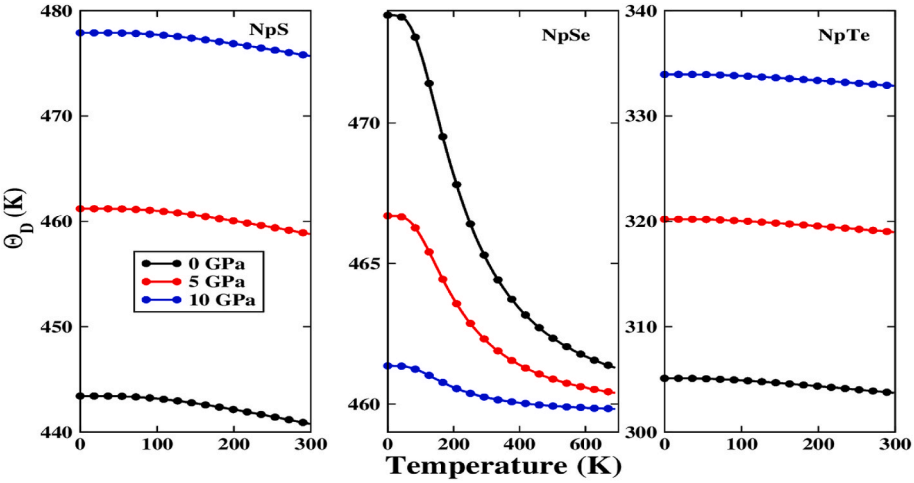

Fig. 13. Debye temperature variation with temperature and pressure of NpX (X = S, Se, Te).

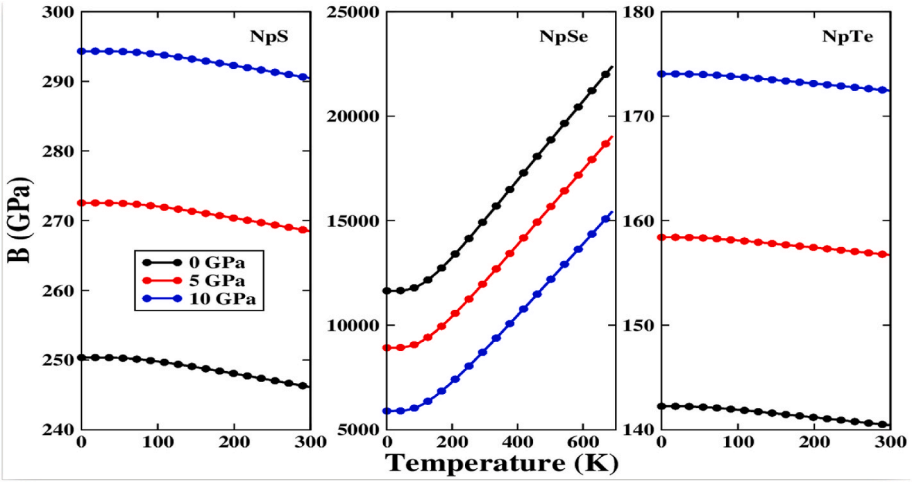

Fig. 14. The change in Bulk modulus with temperature and pressure of NpX (X = S, Se, Te).

pressure for NpS and NpTe compounds, while the Debye temperature decreased with the increase of pressure for NpSe chalcogenide. The value of Debye temperature at ambient pressure and temperature was recorded for NpS, NpSe, and NpTe compounds which were 444, 479, and 306 K respectively. A slight decrease in Debye temperature was noted by increasing the temperature which is due to a change of density of acoustic phonons as it is mainly related to Debye temperature. Bulk modulus is considered a property of a material that defines its resistance to change in volume when it is compressed or stretched. Fig. 14 shows the variation of bulk modulus by the temperature at a given pressure of 0, 5, and 10 GPa. A slightly linear decrease in bulk modulus was noted with an increase in temperature for NpS and NpTe chalcogenides. However, the increase in bulk modulus was noted for NpSe chalcogenide with an increase in temperature. For both NpS and NpTe, the compressibility increases by raising the temperature at a particular pressure. However, the compressibility of both compounds decreases with the increase of pressure at a particular temperature. This type of trend normally occurs because the behavior of the increase of temperature on the material is the same as the decrease of the pressure.

4. Conclusion

In a nutshell, we have theoretically investigated the structural, phonon, electronic, optical, IR optical and thermodynamic properties of NpX, where X = S, Se, Te chalcogenides using full potential linearized augmented plane wave present in the framework of WIEN2k software and pseudopotential approach as implemented in Quantum ESPRESSO. Structural analysis determined that all these compositions belong to face-centered cubic structure with lattice parameter 5.3770 Å for NpS which increased to 5.6168Å and 6.0525 Å when S was replaced with Se and Te. The band structure investigation exposed their conducting nature in both spin channels. The significant contribution of *d* and *f*-states of Np and *p*-states of chalcogens in band formation was evident from the density of state plots. With the increasing size of chalcogen, the absorption edge was shifted towards a lower energy range which supported the decrease in bandgap and feasibility of these compositions for device fabrication in the IR region.

CRediT authorship contribution statement

Abu Bakar: Formal analysis, Data curation, Conceptualization. **Sadam Hussain:** Software, Methodology. **Ghulam M. Mustafa:** Formal analysis, Data curation. **Rana Ali Ahmad:** Formal analysis, Data curation. **Abdul Quader:** Formal analysis. **Muhammad Imran:** Validation. **Ibrahim A. Shaaban:** Writing – review & editing.

Declaration of competing interest

The authors declare that they have no known competing financial interests or personal relationships that could have appeared to influence the work reported in this paper.

Data availability

Data will be made available on request.

Acknowledgment

The authors extend their appreciation to the Research Center for Advanced Materials Science (RCAMS), King Khalid University, Saudi Arabia, for funding this work under grant number RCAMS/KKU/012-22.

References

[1] K.C. Maurya, A. Chatterjee, S.M. Shivaprasad, B. Saha, Morphology-controlled reststrahlen band and infrared plasmon polariton in GaN nanostructures, Nano Lett. 22 (23) (2022) 9606–9613.
[2] K. Feng, W. Streyer, Y. Zhong, A.J. Hoffman, D. Wasserman, Photonic materials, structures and devices for Reststrahlen optics, Opt Express 23 (24) (2015) A1418–A1433.
[3] K. Puneet, S.K. Chakraborty, Infrared radiation: principles and applications in food processing, Thermal Food Engineering Operations (2022) 349–373.
[4] M.C. Anderson, R.G. Allen, A. Morse, W.P. Kustas, Use of Landsat thermal imagery in monitoring evapotranspiration and managing water resources, Rem. Sens. Environ. 122 (2012) 50–65.
[5] D.U. Yildirim, A. Ghobadi, M.C. Soydan, O. Atesal, A. Toprak, M.D. Caliskan, E. Ozbay, Disordered and densely packed ITO nanorods as an excellent lithography-free optical solar reflector metasurface, ACS Photonics 6 (7) (2019) 1812–1822.
[6] T. Kimoto, Material science and device physics in SiC technology for high-voltage power devices, Jpn. J. Appl. Phys. 54 (4) (2015) 040103.
[7] G. Ariyawansa, A.G.U. Perera, X.H. Su, S. Chakrabarti, P. Bhattacharya, Multi-color tunneling quantum dot infrared photodetectors operating at room temperature, Infrared Phys. Technol. 50 (2–3) (2007) 156–161.
[8] B. Wu, L. Cao, Z. Zhang, Q. Fu, Y. Xiong, Terahertz electro-optic sampling in thick ZnTe crystals below the reststrahlen band with a broadband femtosecond laser, IEEE Transactions on Terahertz Science and Technology 8 (3) (2018) 305–311.
[9] X. Wei, X. Zhang, W. Wu, N. Deng, G. Wang, Scattering of A1 (TO1) phonon-polaritons in terahertz range for $LiNbO_3$, in: Photonics for Energy, Optica Publishing Group, 2018, October, pp. PT4B–8.
[10] D.H. Wu, J.R. Meyer, Terahertz emission, detection, and military applications, Terahertz for Military and Security Applications II 5411 (2004, September) 187–195. SPIE.
[11] Y. Zhang, Q. Zhou, J. Zhu, Q. Yan, S.X. Dou, W. Sun, Nanostructured metal chalcogenides for energy storage and electrocatalysis, Adv. Funct. Mater. 27 (35) (2017) 1702317.
[12] S. Yue, L. Li, S.C. McGuire, N. Hurley, S.S. Wong, Metal chalcogenide quantum dot-sensitized 1D-based semiconducting heterostructures for optical-related applications, Energy Environ. Sci. 12 (5) (2019) 1454–1494.
[13] C. Kumari, P. Sharma, S.C. Katyal, S. Chhoker, Correlation of optical parameters of pure and doped $Ge_{17}Sb_8Se_{75-x}Er_x$ chalcogenides films using transmission spectra, Opt. Mater. 132 (2022) 112748.
[14] Z. Yang, D. Jia, Y. Wu, D. Song, X. Sun, C. Wang, Q. Shen, Novel lithium-chalcogenide batteries combining S, Se and C characteristics supported by chitosan-derived carbon intertwined with CNTs, Chem. Eng. J. 427 (2022) 131790.
[15] M. Rakshit, D. Jana, D. Banerjee, General strategies to improve thermoelectric performance with an emphasis on tin and germanium chalcogenides as thermoelectric materials, J. Mater. Chem. A 10 (13) (2022) 6872–6926.
[16] T.V. Vu, A.A. Lavrentyev, B.V. Gabrelian, H.D. Tong, V.A. Tkach, O.V. Parasyuk, O. Y. Khyzhun, A theoretical and experimental study of the valence-band electronic structure and optical constants of quaternary copper mercury tin sulfide, Cu_2HgSnS_4, a potential material for optoelectronics and solar cells, Opt. Mater. 96 (2019) 109296.
[17] T.V. Vu, A.A. Lavrentyev, B.V. Gabrelian, V.A. Ocheretova, O.V. Parasyuk, O. Y. Khyzhun, Particular features of the electronic structure and optical properties of Ag_2PbGeS_4 as evidenced from first-principles DFT calculations and XPS studies, Mater. Chem. Phys. 208 (2018) 268–280.
[18] K. Tanaka, M. Oonuki, N. Moritake, H. Uchiki, Cu_2ZnSnS_4 thin film solar cells prepared by non-vacuum processing, Sol. Energy Mater. Sol. Cell. 93 (5) (2009) 583–587.
[19] T.V. Vu, A.A. Lavrentyev, B.V. Gabrelian, O.V. Parasyuk, V.A. Ocheretova, O. Y. Khyzhun, Electronic structure and optical properties of $Ag_2HgSnSe_4$: first-principles DFT calculations and X-ray spectroscopy studies, J. Alloys Compd. 732 (2018) 372–384.
[20] B.V. Gabrelian, A.A. Lavrentyev, T.V. Vu, K.F. Kalmykova, L.N. Ananchenko, V. A. Tkach, O.Y. Khyzhun, Valence-band electronic structure and main optical properties of $Cu_2HgGeTe_4$: theoretical simulation within a DFT framework and experimental XPS study, Mater. Today Commun. 23 (2020) 100828.
[21] T. Zhu, R. He, S. Gong, T. Xie, P. Gorai, K. Nielsch, J.C. Grossman, Charting lattice thermal conductivity for inorganic crystals and discovering rare earth chalcogenides for thermoelectrics, Energy Environ. Sci. 14 (6) (2021) 3559–3566.
[22] A.S. Mathur, S. Upadhyay, P.P. Singh, B. Sharma, P. Arora, V.K. Rajput, B.P. Singh, Role of defect density in absorber layer of ternary chalcogenide Cu_2SnS_3 solar cell, Opt. Mater. 119 (2021) 111314.
[23] R.A. Kowalski, J.R. Nolen, G. Varnavides, S.M. Silva, J.E. Allen, C.J. Ciccarino, J. D. Caldwell, Mid-to Far-Infrared Anisotropic Dielectric Function of HfS_2 and $HfSe_2$, Adv. Opt. Mater. 10 (23) (2022) 2200933.
[24] A. Heßler, I. Bente, M. Wuttig, T. Taubner, Ultra-thin switchable absorbers based on lossy phase-change materials, Adv. Opt. Mater. 9 (24) (2021) 2101118.
[25] M.Y. Valakh, A.P. Litvinchuk, V.M. Dzhagan, V.O. Yukhymchuk, Y.O. Havryliuk, M. Guc, D.R.T. Zahn, Optical properties of quaternary kesterite-type $Cu_2Zn(Sn_{1-x}Ge_x)S_4$ crystalline alloys: Raman scattering, photoluminescence and first-principle calculations, RSC Adv. 6 (72) (2016) 67756–67763.
[26] G. Schreckenbach, P.J. Hay, R.L. Martin, Density functional calculations on actinide compounds: survey of recent progress and application to [UO2X4] 2−(X= F, Cl, OH) and AnF6 (An= U, Np, Pu), J. Comput. Chem. 20 (1) (1999) 70–90.

[27] P. Blaha, K. Schwarz, G. Madsen, D. Kvasnicka, J. Luitz, An Augmented Plane Wave + Local Orbitals Program for Calculating Crystal Properties;user Guide, Wien2K (18.2), Vienna University of Technology., 2018, p. 8.
[28] P. Giannozzi, S. Baroni, N. Bonini, M. Calandra, R. Car, C. Cavazzoni, R. M. Wentzcovitch, Quantum ESPRESSO: a modular and open-source software project for quantum simulations of materials, J. Phys. Condens. Matter 21 (39) (2009) 395502.
[29] J.P. Perdew, K. Burke, M. Ernzerhof, Generalized gradient approximation made simple, Phys. Rev. Lett. 77 (18) (1996) 3865.
[30] H.J. Monkhorst, J.D. Pack, Special points for Brillouin-zone integrations, Phys. Rev. B 13 (12) (1976) 5188.
[31] A. Dal Corso, A.M. Conte, Spin-orbit coupling with ultrasoft pseudopotentials: application to Au and Pt, Phys. Rev. B 71 (11) (2005) 115106.
[32] T.P. Cysne, A. Ferreira, T.G. Rappoport, Crystal-field effects in graphene with interface-induced spin-orbit coupling, Phys. Rev. B 98 (4) (2018) 045407.
[33] M. Aras, Ç. Kılıç, S. Ciraci, Magnetic ground state in FeTe 2, VS 2, and NiTe 2 monolayers: antiparallel magnetic moments at chalcogen atoms, Phys. Rev. B 101 (5) (2020) 054429.
[34] M. Aynyas, A. Rukmangad, B.S. Arya, S.P. Sanyal, Phonon dynamics of neptunium chalcogenides, Journal Conference Proceedings 1447 (2012, June) 801 [34] Kumar, A., & Ahluwalia, P. K. (2012). Tunable dielectric response of transition metals dichalcogenides MX_2 (M= Mo, W; X= S, Se, Te): Effect of quantum confinement. Physica B: Condensed Matter, 407(24), 4627-4634.
[35] A. Kumar, P.K. Ahluwalia, Tunable dielectric response of transition metals dichalcogenides MX2 (M= Mo, W; X= S, Se, Te): effect of quantum confinement, Phys. B Condens. Matter 407 (24) (2012) 4627–4634.
[36] K. Anshu, A. Sharma, Study of Se based quaternary SePb (Bi, Te) chalcogenide thin films for their linear and nonlinear optical properties, Optik 127 (1) (2016) 48–54.
[37] P.K. Singh, D.K. Dwivedi, Chalcogenide glass: fabrication techniques, properties and applications, Ferroelectrics 520 (1) (2017) 256–273.
[38] S. Nakov, E. Sobakinskaya, F. Müh, A unified framework for the numerical evaluation of the Q-subtractive Kramers–Kronig relations and application to the reconstruction of optical constants of quartz, Spectrochim. Acta Mol. Biomol. Spectrosc. 288 (2023) 122157.